

# Identifying anomalous radio sources in the EMU Pilot Survey using a complexity-based approach

Gary Segal,<sup>1,2\*</sup> David Parkinson,<sup>3†</sup> Ray Norris,<sup>2,4</sup> Andrew M. Hopkins,<sup>5</sup> Heinz Andernach,<sup>6</sup> Emma L. Alexander,<sup>7</sup> Ettore Carretti,<sup>8</sup> Bärbel S. Koribalski,<sup>2,4</sup> Letjatji S. Legodi,<sup>9</sup> Sarah Leslie,<sup>10</sup> Yan Luo,<sup>11</sup> Jonathon C. S. Pierce,<sup>12</sup> Hongming Tang,<sup>13</sup> Eleni Vardoulaki,<sup>14</sup> Tessa Vernstrom<sup>15</sup>

<sup>1</sup>*School of Mathematics and Physics, University of Queensland, St Lucia, Brisbane, QLD 4072, Australia*

<sup>2</sup>*CSIRO Space and Astronomy, PO Box 76, Epping, 1710, NSW, Australia*

<sup>3</sup>*Korea Astronomy and Space Science Institute, Daejeon 34055, Korea*

<sup>4</sup>*Western Sydney University, Locked Bag 1797, Penrith, NSW 2751, Australia*

<sup>5</sup>*Australian Astronomical Optics, Macquarie University, 105 Delhi Rd, North Ryde, NSW 2113, Australia*

<sup>6</sup>*Departamento de Astronomía, Universidad de Guanajuato, Callejón de Jalisco s/n, Guanajuato, C.P. 36023, GTO, Mexico*

<sup>7</sup>*Jodrell Bank Centre for Astrophysics, Department of Physics and Astronomy, University of Manchester, Manchester, UK*

<sup>8</sup>*INAF, Istituto di Radioastronomia, Via Gobetti 101, 40129 Bologna, Italy*

<sup>9</sup>*South African Radio Astronomy Observatory, 2 Fir Street, Black River Park, Observatory, Cape Town, 7925, South Africa*

<sup>10</sup>*Leiden Observatory, Leiden University, PO Box 9513, NL-2300 RA Leiden, The Netherlands*

<sup>11</sup>*School of Physics and Astronomy, Sun Yat-sen University, 2 Daxue Road, Zhuhai 519082, China*

<sup>12</sup>*Centre for Astrophysics Research, University of Hertfordshire, College Lane, Hatfield AL10 9AB, UK*

<sup>13</sup>*Department of Astronomy, Tsinghua University, Beijing 100084, China*

<sup>14</sup>*Thüringer Landessternwarte, Sternwarte 5, 07778 Tautenburg, Germany*

<sup>15</sup>*ICRAR, The University of Western Australia, 35 Stirling Hwy, 6009 Crawley, Australia*

Accepted XXX. Received YYY; in original form ZZZ

## ABSTRACT

The Evolutionary Map of the Universe (EMU) large-area radio continuum survey will detect tens of millions of radio galaxies, giving an opportunity for the detection of previously unknown classes of objects. To maximise the scientific value and make new discoveries, the analysis of this data will need to go beyond simple visual inspection. We propose the coarse-grained complexity, a simple scalar quantity relating to the minimum description length of an image, that can be used to identify images that contain complex and unusual structures. The complexity can be computed without reference to the ensemble or existing catalogue data, making the computation efficient on surveys at very large scales (such as the full EMU survey). We apply our coarse-grained complexity measure to data from the EMU Pilot Survey to detect and confirm anomalous objects in this data set and produce an anomaly catalogue. Rather than work with existing catalogue data using a specific source detection algorithm, we perform a blind scan of the area, computing the complexity using a sliding square aperture. The effectiveness of the complexity measure for identifying anomalous objects is evaluated using crowd-sourced labels generated via the Zooniverse.org platform. We find that the complexity scan captures unusual sources, such as odd radio circles, in the high-value tail of the complexity distribution. We use this distribution to produce catalogues of the 5%, 1% and 0.5% most complex frames with the largest catalogue estimated to be 86% complete and the smallest catalogue 94% pure.

**Key words:** radio continuum: galaxies – surveys – galaxies: statistics

## 1 INTRODUCTION

The large-scale analysis of the extragalactic sky has, in the past, delighted astronomers with new and unusual objects. We have no doubt that it will continue to do so into the future, with new large-

\* E-mail: g.segal@uq.edu.au

† Email: davidparkinson@kasi.re.kr

scale surveys such as the Legacy Survey of Space and Time (Ivezic et al. 2019, LSST), Dark Energy Spectroscopic Instrument (DESI Collaboration et al. 2016, DESI), Evolutionary Map of the Universe (Norris et al. 2011, EMU), LOFAR Two-metre Sky Survey (Shimwell et al. 2022, 2017, LoTSS), Spectro-Photometer for the History of the Universe, Epoch of Reionization, and Ices Explorer (Doré et al. 2014, SPHEREx), and the Square Kilometre Array (Dewdney et al. 2009, SKA), either in operation or starting very soon. The work of the astrophysicist is to understand these objects, learn their nature, and identify if they fall inside some already understood class, or constitute an entirely new type of object. For objects that have features or attributes that are completely unexpected, so called ‘unknown unknowns’, even detecting these in the first place may be a challenge. In the present paper we define an anomaly, in broad terms, as an observation that is considered unexpected, based on consensus votes from astrophysicists.<sup>1</sup> While a human may easily notice something that is unexpected, training a machine to do so may be more difficult. The application of machine learning approaches such as outlier detection to astrophysics has already seen some developments with a number of different algorithms or approaches (e.g. Mostert et al. (2021); Giles & Walkowicz (2020)). The complexity based approach offers a computationally efficient alternative to outlier detection based on the morphology of radio sources.

The effectiveness of machine learning approaches, such as Convolutional Neural Networks, have been demonstrated for identifying and classifying observations in astronomical surveys based on their features (Aniyan & Thorat 2017; Lukic et al. 2018, 2019; Karpenka et al. 2013; Kim & Bailer-Jones 2016; Kessler et al. 2010; Dieleman et al. 2015; Huertas-Company et al. 2015; Charnock & Moss 2017; Wu et al. 2019; Lochner et al. 2016). Unsupervised learning approaches, such as self-organising maps, have also been applied to clustering and segmentation problems including PINK by Polsterer et al. (2019) and applications by Galvin et al. (2020); Mostert et al. (2021); Gupta et al. (2022). Lochner & Bassett (2021) developed Astronomaly as a general anomaly detection framework based on an active learning approach that provides personalised recommendations. Astronomaly (Lochner & Bassett 2021) was designed to work with a broad range of astronomical data from images to spectra. Lochner & Bassett (2021) used a Galaxy Zoo project to demonstrate the effectiveness of the approach, where Astronomaly was found to double the number of interesting objects found within the first 100 viewed within the datasets.

In our original paper (Segal et al. (2019), hereafter S19), we introduced the idea of the coarse-grained complexity measure as a tool for identifying complex and anomalous objects. This quantity was based on the notions of *effective complexity* defined by Gell-Mann (1994) and *apparent complexity* defined and implemented in Aaronson et al. (2014), as a coarse-grained description of the information inherent in the possible states of a system.<sup>2</sup> In S19 we used data from the Australia Telescope Large Area Survey (ATLAS), to measure the coarse-grained complexity of radio continuum images using the `gzip` (Levine 2012) byte length to estimate the upper bound of the complexity value. We found it to be useful (when

<sup>1</sup> Similar to the threshold suggested by the United States Supreme Court Justice Potter Stewart

<sup>2</sup> Random intensity fluctuations (noise) cannot be compressed and will increase the description length required to represent possible states beyond those generated by the source object. This noise does not describe the complexity of the object of interest and is reduced through smoothing as part of the measurement of the coarse-grained complexity.

combined with clustering methods to automate the process) for segmenting complex or unusual images from simple images without requiring large training data and without reference to specific features or source specific training labels. The approach generalised well when applied to new data after being calibrated on a much smaller dataset, and has worst-case linear time complexity<sup>3</sup>.

There were, however, some limitations we noted using this very simple approach. The implementation in S19 used `gzip` as the compression algorithm, which resulted in small variations in the complexity computed when the inputs were rotated. `gzip` uses the flattened image as an input in our implementation, and this will differ based on the rotational orientation of the original two dimensional image. Furthermore, there is no reason why Lempel-Ziv encoding, originally designed to compress a one-dimensional data stream, should be optimal in compressing astronomical images. To address these limitations in our original approach, in this new work we consider calculating the coarse-grained complexity using Autoencoders (AE), based on modern deep learning methods. Autoencoders, if implemented effectively, can preserve the desired features from the data while remaining invariant to affine transformations such as rotation, by learning to retain optimal information in the lower dimensional latent space.

AE have been applied to various types of astronomical data, including exploring galaxy spectra (Portillo et al. 2020) and Bayesian parameter estimation for gravitational wave astronomy (Gabbard et al. 2022). There have been a number of recent attempts to use AE to generate radio galaxy samples with known labels and classifying galaxy morphology. Ma et al. (2018) used AE and Gaussian mixture models (GMMs) to generate morphology for Fanaroff-Riley type-I (FRI) and type-II (FRII) radio galaxies with high efficiency. Nishikawa-Toomey et al. (2020) developed a Variational Autoencoder (VAE) with Equivariant Transformer layers (with a classifier network from the latent space) that provided promising results when applied to the Galaxy Zoo data set. They found that pre-training the classifier network using unlabelled data resulted in higher accuracy.

Cheng et al. (2021) explored the use of AE for galaxy morphology analysis using a combination of feature extraction and hierarchical clustering (HC) within a novel vector-quantised variational autoencoder (VQ-VAE). Comparing the clusters generated by the HC approach with classic Hubble types (ellipticals, lenticulars, early spirals, late spirals, and irregulars), they argue that there is an intrinsic vagueness in visual classification systems, in particular galaxies with transitional features such as lenticulars and early spirals. They further argue that the proposed method matches visual classifications and physical properties, as well as provides an independent classification that is physically meaningful.

Ralph et al. (2019) used AE as part of a pipeline for data exploration and clustering of morphologies for radio images. They used an AE to reduce the dimensionality of the input data and to help ensure that the compressed representations were affine-transform invariant. The compressed representations were then used to train

<sup>3</sup> The worst-case time complexity refers to an upper bound on the time to run an algorithm by counting elementary operations for all permissible inputs. The efficiency of the algorithm is evaluated based on the order of growth (e.g. logarithmic, linear, quadratic, etc) of the worst-case time complexity with respect to the increasing size of the input. The worst-case running time of a linear time complexity algorithm will increasingly linearly with the sample size. Typically algorithms that rely on ‘between member’ operations within an ensemble (such as a classic Self-organising Map Algorithm) will have running times that scale (at least) quadratically with increasing sample size.

a self-organizing map (SOM) to create a similarity matrix of the input data. They then used kmeans clustering to assign labels using the similarity maps. Finally the Dimensionality Reduction Anomaly Meta-Algorithm (Vafaei Sadr et al. 2021, DRAMA) uses AE and VAE as possible dimensionality reduction techniques as part of the procedure for anomaly detection.

All of these approaches are using AE to break down the image into some form of representation, and then use the properties of this representation to either sort, classify, reconstruct, or identify objects that do not match.

The complexity approach used in the present paper is very similar, in that it uses a property of the encoded image to sort or partition between common and unusual objects. But it uses the simplest property of the representation, that is, the length of the representation, encoded in bits.

In this paper we develop an autoencoder trained to specifically encode the type of images that we would expect for radio continuum surveys such as EMU. Here the latent space that encodes the image can be segmented by layer and intensity values in three parts: *source encoding* (states in the image generated by the physical objects such as extended radio sources), *noise encoding* (states generated by random processes in the imaging procedure), *discard encoding* (states common to all images encoded in this fashion). The size in bits of the source encoding segment can then be used as a coarse-grained complexity measure, while the size of the noise segment can be interpreted as a measure of the noise level.

We implemented our new method on data from the Pilot Survey of the Evolutionary Map of the Universe (EMU-PS, Norris et al. (2021b)). While the primary goal of the EMU Pilot Survey is to test and refine observing parameters and strategy for the main survey, the EMU-PS in itself presents opportunity for new discoveries. Recently self-organising maps have been used successfully to detect unusual sources with reference to the ensemble using a subset of components from complex sources selected from EMU-PS catalogue data (Gupta et al. 2022). The method used in the present paper computes a complexity measure that does not make reference to the ensemble or require a catalogue. We partition the data into frames rather than sources, computing the coarse-grained complexity within a sliding frame (square aperture) across the image. An important feature of the scan method used is that the frames are sampled from the EMU-PS data in a blind manner (that is without using a source extraction tool or existing catalogue data). This helps reduce the risk of producing a sample that is biased towards preconceived notions of what is interesting, referred to as expectation bias by Norris (2017) and Robinson (1987). The approach can also be used without the prior identification of complex sources. This is intended to assist with the identification of the unexpected in new and large data with the goal of new scientific discoveries and surprise.

We evaluated the effectiveness of the approach at finding new and unusual objects by using a Zooniverse project to produce crowd-sourced (from amongst astrophysicists) labels for frames produced by the scan. These labels can be used to generate a partition boundary for anomalies which can be used to create an anomaly catalogue. An effective anomaly partition is an intended product from this work, providing: a concentrated search space, rich in unusual or anomalous objects, intended to provide an efficient tool for assisting with scientific analysis and new discoveries. While not every object in the anomaly catalogue will necessarily be truly ‘anomalous’, the aim is to produce a catalogue where almost all contained frames will be interesting in some fashion (i.e. complex or unusual).

This paper proceeds as follows: in section 2 we describe the theoretical foundations for the coarse-grain complexity measure and

show how it can be practically computed. We also outline how the approach can be implemented using convolutional autoencoders to benefit from some of the advantages of deep learning approaches, including the ability to train models on transformed inputs to help make the approach invariant to affine transformations such as rotation, overcoming a potential limitation with the approach adopted in S19.

In section 3 we introduce the EMU-PS data as a test case for using the coarse-grained complexity measure to identify anomalous objects in future large-scale surveys. The EMU-PS data is likely to contain many rare, unusual and anomalous objects, providing a better representation of the complexity tail of still much larger future surveys (compared to the S19 analysis). It is in this tail that future discoveries are likely to be made.

Section 4 outlines the methods and experiments where we use complexity to analyse radio images. This section details results from reanalysis of the Australia Telescope Large Area Survey (ATLAS) data used in S19, where we compare approaches implemented previously with the measurement of coarse-grained complexity using the convolutional autoencoder described in section 2. These results demonstrate the effectiveness of the approach in identifying complex (multiple component) and unusual sources but also show little benefit in adopting the convolutional autoencoder over the original measurement approach implemented in S19. This section then details the scanning methodology applied to the EMU-PS and concludes by showcasing a variety of frames captured in the complexity tail containing complex structures and unusual objects.

Section 5 details the use of a Zooniverse project to crowd-source labels for EMU-PS frames which are then used to determine an effective coarse-grained complexity partition that can be used to identify complex and unusual objects. Performance measurement is discussed in detail along with the methods and challenges involved in sub-sampling from the very large number of frames produced by the EMU-PS complexity scan. We discuss the challenges in producing an effective sub-sample for evaluating the complexity measure, which needs to be small enough to be efficiently evaluated by a reasonable number of Zooniverse volunteers, while still large enough to provide an effective representation of the tail of the complexity distribution. Section 5 also evaluates the effectiveness of alternative partition boundaries, and details the application of these boundaries in constructing anomaly catalogues, which are produced using the EMU-PS data. This section concludes with a discussion of potential classification errors and considerations.

Section 6 of the paper provides a brief summary and outlines the key outputs and conclusions drawn from this work.

## 2 COARSE-GRAINED COMPLEXITY

In this section we describe the theoretical foundations for the coarse-grained complexity measure and show how it can be practically computed. We also outline how the approach can be implemented using convolutional autoencoders to benefit from some of the advantages of deep learning approaches, including the ability to train models that are invariant to affine transformations such as rotation, overcoming a potential limitation with the approach adopted in S19.

### 2.1 Theoretical basis

The coarse-grained complexity as defined in S19 is based on the notions of *effective complexity* (Gell-Mann 1994) and *apparent complexity* (Aaronson et al. 2014). The apparent complexity is a

measure of the entropy  $H$  of an object  $x$  computed after applying a smoothing function  $f$ , expressed as  $H(f(x))$ . The Shannon entropy of a probability distribution  $P$  can be defined as the expected number of random bits that are required to produce a sample from that distribution:

$$H(P) = - \sum_{x \in X} P(x) \log P(x). \quad (1)$$

By Shannon's Noiseless Coding Theorem the minimum average description length  $L$  of a sample is close to the Shannon entropy:

$$H(P) \leq L \leq H(P) + 1. \quad (2)$$

The Kolmogorov complexity  $K(f(x))$  can be used as a proxy for the entropy of the smoothed function  $H(f(x))$ , as proposed by [Aaronson et al. \(2014\)](#). The analogy between the concept of entropy and program size has been previously recognised ([Chaitin 1975](#)). The Kolmogorov complexity of  $x$  is the length of the shortest binary program  $l(p)$ , for the reference universal prefix Turing machine  $U$ , that outputs  $x$ ; it is denoted as  $K(x)$ :

$$K(x) = \min_p \{l(p) : U(p) = x\}. \quad (3)$$

A thorough treatment is provided by [Li & Vitanyi \(2008\)](#). The Kolmogorov complexity has the advantage of being well-defined for a particular description of a system such as an image of a galaxy. This is not the case for the Shannon entropy which is defined in terms of the possible states of the system. While the Kolmogorov complexity is uncomputable, its upper bound can be reasonably approximated by the compressed file size  $C(f(x))$  using a standard compression program ([Aaronson et al. 2014](#)), such as `gzip`.

The issue with using the approximated Kolmogorov complexity directly as a measure of complexity is that it is maximised by random information. Intuitively a complexity measure should provide low values for random data that does not contain structure that is of interest to the observer ([Zenil et al. 2012](#)). [Aaronson et al. \(2014\)](#) have shown that the apparent complexity measure is able to achieve this by applying a smoothing function  $f$  to the input  $x$  (which removes fine-grained noise while preserving the coarse-grained structure of the image). While the Kolmogorov complexity of a random sequence is large, the apparent complexity of the same sequence becomes small with smoothing, as fluctuations are removed where the average or median information content becomes homogeneous at the coarse-grained resolution. Accordingly we define the coarse-grained complexity, equivalent to the apparent complexity, as the compressed description of regularities and structure after discarding all that is incidental. The coarse-grained complexity will be small for both simple and random sequences.

The objective of applying the smoothing function  $f$  when deriving  $C(f(x))$  is to remove incidental or random information, such as instrumental noise, that is incomprehensible to the observer even though it may have a physical basis. Comprehensibility here is defined with respect to the observer of the information, in this case scientists with specific interests. Comprehensible information has a structure within a feature space, which in the case of images refers to the spatial distribution of bits of information across available channels. The coarse-grained complexity measure extends the idea of the apparent complexity, to incorporate calibration in alignment with expert distinctions between meaningful structure and noise, by adjusting the measurement resolution through a smoothing function so that complexity values correctly partition data that has been expertly labelled (i.e. by human astronomers).

Importantly, the coarse-grained complexity measure of an image does not rely on the presence of any particular structures or

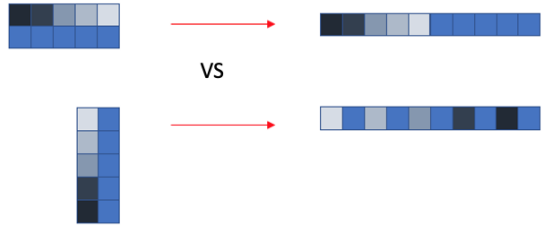


**Figure 1.** `gzip` is not invariant under all affine transformations as it reads the input as a flattened string that differs based on the rotational orientation of the two dimensional input image.

structural elements and is invariant under most rigid motions. The measure makes only explicit assumptions regarding the choice of the coarse-graining level and the scale of the image. Previous data are therefore used only to calibrate the coarse-graining level (i.e. the appropriate measurement resolution) and only a small sample of the relevant data type is required.

Coarse-grained complexity runs into obstacles as a well-defined measure of complexity. Firstly, the uncomputability of the Kolmogorov complexity prohibits the concept from being defined in terms of an optimal compression. It has been proven by [Chaitin et al. \(1995\)](#) that there can be no procedure for finding all theorems that would allow for further compression. Furthermore the problem of distinguishing between meaningful structure and incidental information, especially in finite data, may fail to be well-defined. Different smoothing functions and different coarse-graining levels will retain different distinct regularities in the data.

These theoretical challenges in objectively defining the coarse-grained complexity can be circumvented when the approach is applied to the segmentation of observations by complexity. Here the coarse-grained complexity can be calibrated to coincide with notions of complexity adopted by the observer (i.e. expert astronomers).

## 2.2 Complexity computation

The approach implemented in S19 used `gzip`, based on Lempel-Ziv (LZ77) and Huffman coding, as the compression algorithm. The choice of compression algorithm was consistent with experiments previously implemented by [Aaronson et al. \(2014\)](#). The adoption of a lossless compression approach also avoided information loss outside of the calibration of the smoothing function. The calibration of the smoothing function is intended to align with a coarse-grained resolution where meaningful structure is apparent and noise is reduced. The coarse-grained complexity, as implemented in S19, can be efficiently computed at worst-case linear time complexity:

$$T(n) = O(n) \quad (4)$$

A drawback of the approach, however, is that `gzip` was not designed to compress astronomical images and is not invariant to rotations. `gzip` was created to compress one-dimensional data streams, and uses the flattened image in our implementation. The computed complexity value will therefore differ based on the rotational orientation of the two dimensional input image, a simple and extreme case is illustrated in figure 1.

To overcome these issues we implemented the apparent complexity using Autoencoders (AE), based on modern deep learning

methods, which if implemented effectively using appropriate training data, preserve the desired features from the data while remaining invariant to affine transformations, by learning to retain optimal information in the lower dimensional latent space.

### 2.2.1 Autoencoders

AE, in a modern computer science context, refer to models that use deep learning approaches to reduce the dimensionality of data (encoding) in such a way that data generated (decoding) from the encoded data (latent space) is as similar as possible to (or retains key features from) the input. In this sense an AE provides lossy data compression in its latent space.

This provides a robust numerical alternative to traditional statistical methods, such as principal component analysis (PCA, as an AE is not constrained to linear projections on an optimal orthonormal basis. Variational autoencoders (VAE) encode and decode probabilistically by sampling from a latent space that varies smoothly through parametrisation of a multivariate distribution.

The latent space can provide a compressed representation of information describing the relevant features of the original data and can be used to compute the coarse-grained complexity. We implemented this approach by learning optimal parameters for encoding and decoding CNNs, via Stochastic Gradient Descent, through minimisation of the reconstruction error using a Binary Cross Entropy loss function. Inputs were normalised (0-1) so Binary cross entropy could be applied as follows:

$$H(y, p) = - \sum y \log p + (1 - y) \log(1 - p), \quad (5)$$

The final convolution layer of the decoder was a sigmoid activation function:

$$\theta(z) = \frac{1}{1 + e^{-z}}, \quad (6)$$

Convolution operations were performed using the learned weights, bias terms and activation function (non-linear). *Same padding* was used to preserve the input dimension per filter (i.e. depth). Pooling layers were used to reduce the resolution and remove noise through average pooling. The architecture of the CNN used to encode astronomical images is shown in figure 2.

Input images, at 64x64 or 256x256 pixels, were reconstructed from a 8x8x64 or 16x16x64 latent space, corresponding to the size of the input image. This latent space contains the information used to re-construct the full image, and is represented in figure 2 by the fourth block from the left, where the autoencoder operations end before decoding starts. This latent space can then be segmented by layer and intensity values, using Gaussian Mixture Models (GMMs) and calibration data. We use this process to extract layer and intensity value information, important to the apparent physical object only and not residual noise, through label segmentation in the calibration data. Thus, the image description encoded in the latent space was segmented in three ways: *source encoding* (states in the image generated by the physical objects such as galaxies), *noise encoding* (states generated by random processes in the imaging procedure), *discard encoding* (states common to all images encoded in this fashion). The size in bits of the source encoding segment was used as a complexity measure, while the size of the noise segment was interpreted as a measure of the noise level.

## 3 EMU PILOT SURVEY DATA

The Pilot Survey of the Evolutionary Map of the Universe (EMU-PS) was observed at 944MHz using the Australian Square Kilometre Array Pathfinder (ASKAP) telescope. The ASKAP telescope consists of 36 12-metre antennas spread over a region 6-km in diameter at the Murchison Radio Astronomy Observatory in Western Australia. EMU-PS covers 270 square degrees of an area covered by the Dark Energy Survey at a spatial resolution of  $\sim 11\text{--}13$  arcsec (Norris et al. 2021b).

While the primary goal of the EMU Pilot Survey is to test and refine observing parameters and the strategy for the main survey, the pilot in itself presents opportunity for new discoveries. Experience has shown (Norris 2017) that whenever we observe the sky to a significantly greater sensitivity, or explore a significantly new volume of observational phase space, we make new discoveries. This goal has already been demonstrated through the successful identification of a new class of radio object, odd radio circles (ORCS, Norris et al. (2021a); Koribalski et al. (2021); Norris et al. (2022), Figure 6 and 7).

The observations and data reduction for EMU-PS are fully described by Norris et al. (2021b) so here we restrict our description to the data product used in the present paper. The data were taken in 10 overlapping tiles, each covering an area of 30 square degrees. These were then merged while correcting for the primary beam response, to produce a single image covering 270 square degrees. Here we use the “native” resolution product (i.e. not convolved to a common beamsize), giving a synthesised beam of about  $11 \times 13$  arcsec with an rms sensitivity of about  $25 \mu\text{Jy}/\text{beam}$ . Source extraction using the *Selavy* tool (Whiting et al. 2017) found a total of 220,102 radio components, of which 178,821 are “simple sources”, which are either unresolved point sources or can be fitted by a single Gaussian. The remaining 41,181 “complex” sources range from small extended sources to giant radio galaxies, and include a number of objects with complex morphology which are the sources of primary interest in the present paper. However it is important to note that, to avoid bias, the *Selavy* extractions are not used at all in this paper, which instead works directly with the image data.

The EMU-PS data is likely to contain examples of anomalous and unexpected objects, providing a better representation of the complexity tail of still much larger future surveys such as EMU (compared to previous experiments using ATLAS data in S19). It is in this tail that future discoveries are likely to be made.

## 4 THE COMPLEXITY OF RADIO IMAGES

We now apply our method to analyse radio images. We start with a reanalysis of the Australia Telescope Large Area Survey (ATLAS) data used in S19, where we compare the method implemented previously with the measurement of coarse-grained complexity using the convolutional autoencoder described in section 2.2. We then scan the EMU Pilot Survey data, examine the distribution of complexity values for each frame, and showcase a variety of complex and unusual objects captured in the complexity tail.

### 4.1 ATLAS data reanalysis

Australia Telescope Large Area Survey (ATLAS) data consist of deep radio continuum imaging of the Chandra Deep Field South (CDFS) and the European Large Area ISO Survey (ELAIS). The

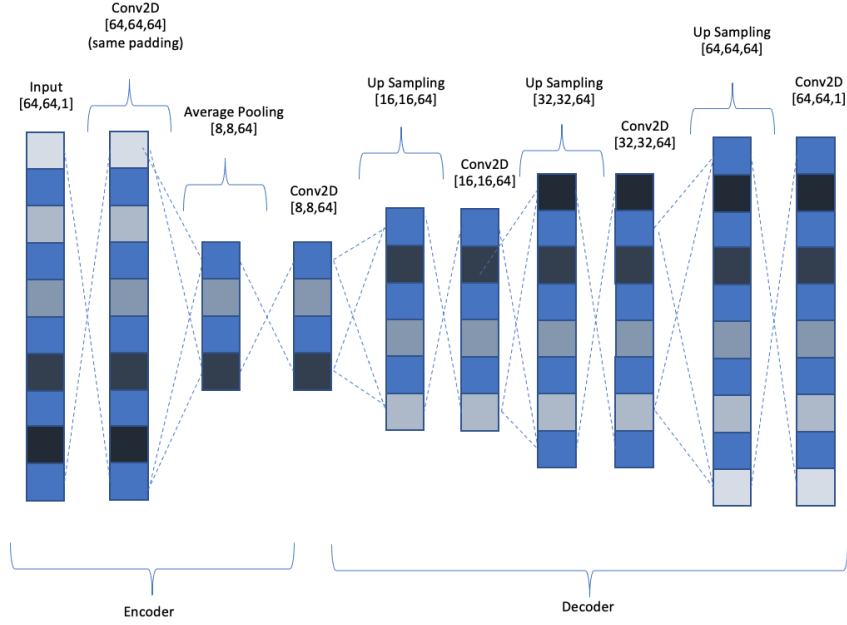


**Figure 2.** 64x64 pixel CNN Autoencoder operations. The same operations scale by a factor of 4 when using 256x256 inputs. The latent space, where the complexity is measured, is the fourth block from the left, where the autoencoder operations end before decoding starts.

DR3 (n=4825)	Complex obs	Simple obs
ELAIS	72	1892
CDFS	97	2764
<hr/>		
DR1 (n=708)	Complex obs	Simple obs
CDFS	34	674

**Table 1.** ATLAS DR1 and DR3 samples

data sets are described in [Norris et al. \(2006\)](#), [Middelberg et al. \(2008\)](#) (DR1), and [Franzen et al. \(2015\)](#) (DR3).

The ATLAS sources used were pre-processed as detailed in [Norris et al. \(2006\)](#) and [Franzen et al. \(2015\)](#). Table 1 shows the number of identified radio sources within each field and data release. The table also provides a breakdown between sources that have been classified by human inspection from [Norris et al. \(2006\)](#) and by the authors of the present paper as having a simple or complex morphology.

Segmentation based on coarse-grained complexity can be used to distinguish between simple and complex radio sources. Here we define “simple” sources as single unresolved components, and “complex” sources as anything else, including bent-tail galaxies and extended radio sources (e.g. Fanaroff-Riley I, Fanaroff-Riley II) containing bright radio components in combination with diffuse plume-like jets. As described in S19, we perform the segmentation by fitting Gaussian mixture models (GMM) and remove observations with low complexity and signal-to-noise ratio (SNR) values to identify complex sources.

We ran a comparison experiment, performing segmentation to identify complex sources, using the same ATLAS (CDFS) data used in S19. The comparison was made between using `gzip`, as implemented in S19, and the size in bits of the source encoding

segment from the latent space of the AE. The use of the median filter, the smoothing kernel size and the threshold filter remained consistent with S19. The AE was trained using the ATLAS DR1 data.

We found comparable performance between the original results from S19 (using `gzip`) and the updated approach using the AE, as shown in table 2. Both approaches performed better than baseline methods described in S19, namely logistic regression and support vector machines, based on calibration on a small dataset and testing on a larger out-of-sample dataset as shown in table 2. These results demonstrate the effectiveness of the coarse-grained complexity approach in identifying complex structures and unusual sources but also show little benefit in adopting the convolutional autoencoder over the original measurement approach implemented in S19.

## 4.2 Scanning the EMU Pilot Survey

### 4.2.1 Scanning Methodology

We estimate the coarse-grained complexity in terms of *frames* of a fixed size, rather than working with pre-selected sources. After computing the complexity in a frame, it is shifted based on a defined stride length to the right and computed again, progressing in this manner until it overlaps with the edge of the image. Once the frame overlaps with edge of the image it returns to the starting column and is shifted down by the defined stride length, progressing in this manner until the frame overlaps with the lower edge of the image. Figure 3 illustrates the sliding frame and the associated parameters. The choice of frame size, stride length and smoothing kernel size are the only free parameters used in this method.

For the EMU-PS image, a frame is defined to be a  $256 \times 256$  pixel region (equivalent to a span of approximately  $\sim 12$  arcmin) that we slide based on a stride length of 64 pixels. This frame size

Trained on DR1 CDFS (n=708 cross val), Tested on DR3 CDFS (n=2861)			
Method	Completeness	False Positive Rate	Informedness
Logistic regression (using pixel data)	0.99	0.36	0.63
SVM (using pixel data)	0.61	0.03	0.58
Complexity (measured using gzip and SNR)	0.86	0.05	0.81
Complexity (measured using AE latent space)	0.94	0.14	0.80

**Table 2.** Comparison of original results from S19 and results measuring the source and noise encoding segments of the AE latent space. The first 3 rows contain results from S19 and the final row contains new results. The terms used in the column headings are defined below in Section 5.3.

exceeds the angular size of most known radio sources in the EMU-PS field, with the exception of a few Giant Radio Galaxies such as those shown in Figures 16 and 28 of Norris et al. (2021b).

An important feature of the scan method is that the frames are *blind* samples from the EMU-PS data. This helps reduce the risk of biasing the sample to preconceived notions of what is complex and interesting. It also avoids restricting the sampling to only regions of an image that are already represented in existing catalogue data. As a consequence of this method, many frames will not contain any detectable sources or objects of interest. Conversely, some frames may contain a part of a source but not the entire object. To help minimise this risk, a stride length of one quarter the span of the frame size was selected. The overlapping frames provide better coverage of the EMU-PS data for computing complexity, as they improve the probability of capturing larger complex structures in a single frame.

The smoothing kernel size defines the measurement resolution for the coarse-grained complexity scan. Smoothing is implemented using a median filter  $f$  applied to frames from the EMU-PS image  $x$ . The smoothing kernel size  $h$ , is in this case calibrated to 10 pixels consistent with the learned smoothing kernel size from S19. The kernel size was calibrated using ATLAS DR1 using sources that had been manually classified as simple and complex, where the size was chosen by maximising the difference between the average coarse-grained complexity of observations labelled complex and simple in the DR1 sample. The median filter was selected because it completely removes noise and incidental values in regions predominately without flux measurement (i.e. where no sources are detected) and retains the strength of signals in regions dominated by actual flux measurements. It is also better at preserving edges (than, for example, a Gaussian filter) given the expected noise.

This approach does not control for the distance of objects contained within each frame and accordingly the measurement resolution does not vary depending on the observed scale of sources contained within each frame. Rather this approach provides a consistent evaluation of complexity for each section of sky covered by the sliding window, irrespective of the sources it contains.

The approach is implemented in accordance with the procedure followed in S19 to calculate the coarse-grained complexity within each frame<sup>4</sup>. The same parameters were applied consistently across the entire EMU-PS radio mosaic. Consistent with S19, a pixel intensity threshold is set at the 90th percentile whereby all values below the threshold are set to zero. S19 explores the sensitivity of the method to the threshold value, showing the effectiveness of the threshold selected compared to alternatives. To estimate  $C(f(x))$

<sup>4</sup> Unlike the procedure followed in S19, frames are not cropped. Instead he complexity is computed for the entire  $256 \times 256$  pixel frame.

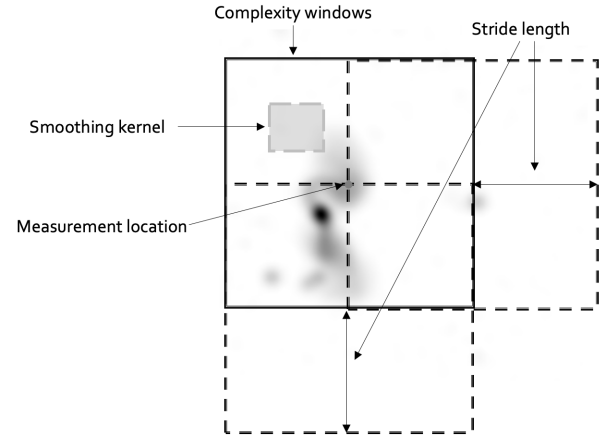


**Figure 3.** The definition of frame size (side length of solid black square), stride length (offset between position of solid black square and dashed black squares) and smoothing kernel size (grey shaded rectangle). The size of the complexity frame is chosen such that most (but not all) extended sources will be fully contained. The stride length is chosen to be one quarter of the side length of the frame, however the illustration above depicts one half for illustrative purposes only. These are the only free parameters used in this scanning method.

as an upper bound on the Kolmogorov complexity  $K(f(x))$  we calculate the size in bits of the gzip compressed image. The signal-to-noise ratio was calculated using the reciprocal of the coefficient of variation for the smoothed array as was implemented in S19. This produces comparable results to using the AE latent space and calculating the size in bits of the source encoding segment as described in Section 2.2.1. Using the AE the residual noise can be measured based on the size in bits of the noise segment.

#### 4.2.2 EMU-PS scan results

We performed a complexity scan of the EMU-PS data using the method described above. The distribution of complexity values from each sampled frame is shown in figure 4. Complexity values are shown in figure 5 as a heat map overlaid on the EMU-PS field.

Visual inspection of a sub-sample of frames shows that the high-complexity value tail of the distribution comprises unusual, complex and extended objects. Extended sources featured heavily in the tail above the 95th percentile ( $\sim 15,000$  bytes), with wide angle tail galaxies and objects of a more anomalous appearance apparent from above the 99th percentile ( $\sim 16,500$  bytes). Findings demonstrate the effectiveness of this approach in recovering known extended and complex structures. Examples of these objects, sam-

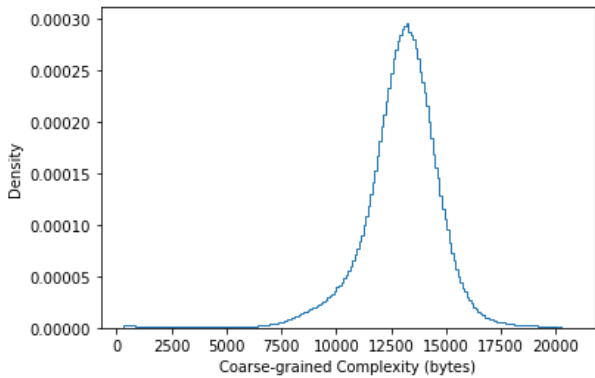


**Figure 4.** Complexity distribution for EMU-PS data after removal of low complexity background data (frames with the minimum complexity value). The left tail contains frames without sources or point sources, predominantly point sources toward the centre.

pled above the 99th percentile, are shown in figure 6. These examples illustrate the breadth of objects found within frames in the high-complexity value tail, including, (a) the unusual source PKS 2130-538 (Otrupcek & Wright 1991) known as the Dancing Ghosts (Norris et al. 2021b) (b) a bright wide angle tail source on 2MASX J21291901-5053040 in cluster Abell 3771, (c) the large X-shaped radio source PKS 2014-55 (2MASX J20180125-5539312), (d) two odd radio circles, EMU PD J205842.8-573658 (ORC2) and EMU PD J205856.0-573655 (ORC3), (e) a face-on spiral galaxy NGC 7125, (f) 2MASX J20483764-4911157 an FR-II remnant, (g) DES J202818.12-492408.4 an FR-I potential double-double radio galaxy and (h) an FR-I extended radio source with host galaxy 2MASX J21512991-5520124. Associated complexity values and additional examples are provided in Appendix A.

The EMU-PS has already produced valuable scientific discoveries, including the identification of a new class of radio object called Odd Radio Circles (ORCs, Norris et al. (2021a); Koribalski et al. (2021); Norris et al. (2022)). Examples, labelled ORC 2 and ORC 3, are shown in the high complexity frames presented in figure 6 (d) and figure 7. ORCs provide examples of recent discoveries coming from EMU-PS that are found in the far right tail of the complexity distribution. The ability of the coarse-grained complexity measure to segment these sources in the distribution tail, in this case above the 99.5th percentile, supports the effectiveness of this approach at identifying scientifically interesting observations in large data in an efficient manner. Being able to capture and segment complex structures and unusual observations in the far right tail provides a smaller and more concentrated search space that can potentially improve the speed and efficiency of making new discoveries. As discussed in S19, the worst-case linear time complexity of the method also makes it computationally efficient to implement.

## 5 IDENTIFYING ANOMALOUS FRAMES

In this section we show how we used a Zooniverse project to crowd-source labels of EMU-PS frames to evaluate the coarse-grain complexity as a measure of interestingness by determining an effective complexity partition. Performance measurement is discussed in detail along with the methods and challenges involved in sub-sampling from the very large number of frames produced by the EMU-PS scan. We evaluate the effectiveness of alternative partition boundaries, and provide details of the application of these boundaries to

construct anomaly catalogues. This section concludes with a discussion of potential classification errors and considerations.

### 5.1 Partitioning the data

To segment the sample and identify interesting observations a partition, or partitions, need to be determined in the tail of the complexity distribution. Drawing a partition at a low complexity value will produce a very large sample. If the goal is to identify complex and unusual objects while minimising the search space for new discoveries (to improve efficiency), then the objective becomes to partition at the largest complexity value that is still exceeded by as many of the most interesting objects as possible.

In S19 the sample was segmented based on the coarse-grained complexity and the signal-to-noise using unsupervised clustering methods (Gaussian Mixture Models), and the results were evaluated using truth labels based on expert classification of the ATLAS data. In the case of the EMU-PS scan we have a much larger sample size of blindly sampled frames, not necessarily containing sources, for which truth labels do not exist. The EMU-PS data covers an area containing approximately 220,000 catalogue sources (Norris et al. 2021b) and the EMU-PS scan contains approximately 365,000 sampled frames. This makes evaluating potential partitions more challenging, as it is not feasible to have experts inspect and classify the hundreds of thousands of frames produced by the scan.

Sub-sampling can be used to make the evaluation of complexity partitions in the EMU-PS data more feasible. Here the data size is reduced by selecting a subset from the original sample. Expert evaluation of this subset is more feasible in shorter time frames.

Effective evaluation of EMU-PS partitions will allow this data to be used to determine an appropriate complexity threshold when using this approach to search new, and even larger surveys, for interesting objects and new discoveries. As an example, the thresholds determined from the EMU-PS data can be used to identify the most interesting frames in the subsequent full EMU survey which is anticipated to capture approximately 40 million sources. As an immediate benefit, this evaluation will also define the threshold for cataloguing frames containing complex structures and unusual objects from the EMU-PS data.

### 5.2 Crowd-sourced evaluation of frames

To provide truth labels for the frames produced by the complexity scan we ran a project on the [Zooniverse.org](https://zooniverse.org) platform, titled “*Anomaly in the EMU Zoo*” (hereafter zoo), requesting expert astronomers to evaluate an unbiased sample of frames sub-sampled from the EMU-PS scan. Consensus from the zoo labels was then used to evaluate the completeness and purity associated with prospective partition boundaries.

Expert volunteers were approached from within the Evolutionary Map of the Universe Survey Project and at the SPARCS 2021 conference. A sub-sample of 1627 frames from the EMU-PS scan ( $n_{\text{total}}=365,000$ ) were presented to volunteers for classification through the Zooniverse project. 44 volunteers participated in the project, with 10 of these classifying more than 500 frames.

The zoo asked the expert volunteers to evaluate the sub-sampled frames and to select an option that best describes the most interesting radio sources in each image before moving on to the next. An example of this workflow is shown in figure 8. The four options presented for selection were:

- No sources/just noise

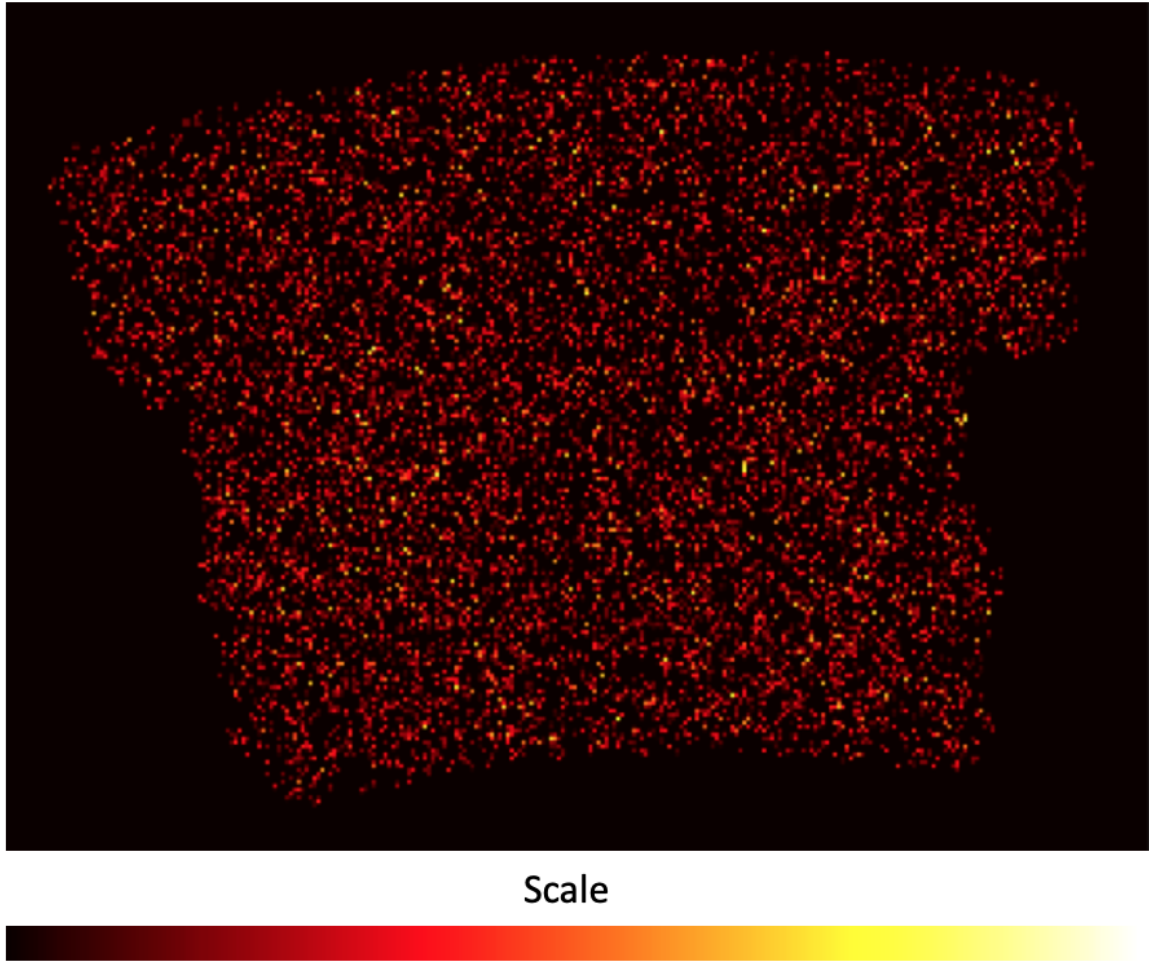


**Figure 5.** A complexity ‘heat map’ of the EMU-PS region, where the complexity of the frame is indicated by the brightness of the pixel. While many of the frames are red coloured, indicating the presence of a simple source, there are a few yellow or white pixels, indicating more complex sources or low-surface brightness structures. The most complex frames seem to be randomly distributed across the survey region, with the exception of the edges, where the noise will be larger.

- One or more simple sources/unrelated simple sources
- At least one complex source/sources with multiple components
- Contains something unexpected/Anomaly

The zoo distinguished between complex and extended sources with multiple components, and sources that were deemed by the volunteers to be truly unexpected or anomalous. This distinction between complex and anomalous sources enabled the evaluation of a complexity threshold that could be used to partition a smaller sample of interesting frames that were very complete with respect to anomalies and also highly pure with respect to anomalies and complex sources. Ensuring that the partitioned data is complete with respect to anomalies supports science objectives for studying and identifying interesting objects that may result in new discoveries. Ensuring the partitioned data is pure with respect to anomalies and more typical complex objects minimises the search space for new discoveries and improves the efficiency when searching for such objects. Retaining more typical complex objects was not seen as an issue, given the potential overlap in the complexity values of more typical complex objects and truly anomalous objects, and

the importance of retaining as many true anomalies as possible. This also helps account for the subjective nature of assigning truth labels, where the complexity value may capture anomalies that are only apparent to some observers.

#### 5.2.1 Using consensus to agree on truth labels

Only frames converging on a label through majority consensus were used to evaluate the effectiveness of the complexity to identify anomalous sources. Those frames from the zoo sample where majority consensus was not reached were excluded from the evaluation. Table 3 shows that 99.8% of the zoo sample frames received evaluations from 3 or more volunteers and 94% from 5 or more. We used the criterion that only frames receiving 5 or more evaluations were used to evaluate consensus, and be given a reliable ‘truth’ label. These restrictions were imposed to avoid the results being impacted by outlier evaluations that differed from the majority of expert volunteers.

The average number of evaluations per frame was 6.85, with

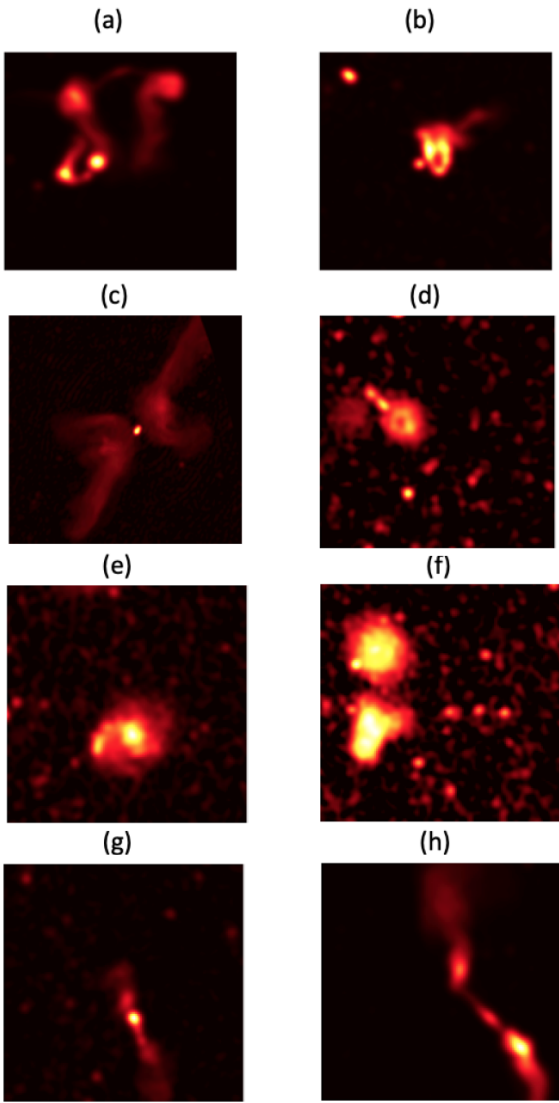


**Figure 6.** Examples of objects found within frames sampled above the 99th percentile complexity value from the EMU-PS Complexity Scan. These examples illustrate the breadth of objects found within frames in the complexity tail including, (a) the unusual source PKS 2130-538 (Otrupcek & Wright 1991) known as the Dancing Ghosts (Norris et al. 2021b), (b) a bright wide angle tail source on 2MASX J21291901-5053040 in cluster Abell 3771, (c) the large X-shaped radio source PKS 2014-55 (2MASX J20180125-5539312), (d) two odd radio circles, EMU PD J205842.8-573658 (ORC2) and EMU PD J205856.0-573655 (ORC3), (e) a face-on spiral galaxy NGC 7125, (f) 2MASX J20483764-4911157 FR-II remnant, (g) DES J202818.12-492408.4 FR-I potential Double-double radio galaxy and (h) FR-I extended radio source with host galaxy 2MASX J21512991-5520124.

a relatively even number of average evaluations across the outcome labels as shown in Table 4. Table 4 also shows that where an outcome label was assigned, the average consensus level was 70% or greater. The number of zoo sample frames converging on a majority consensus in each class is shown in table 5.

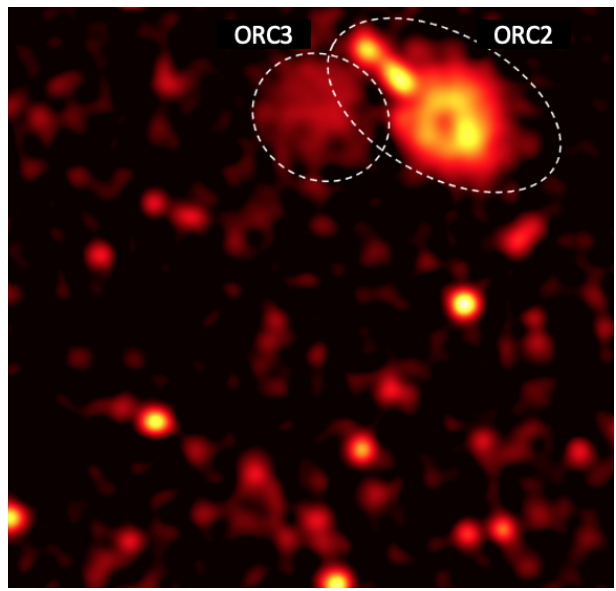


**Figure 7.** An example frame with a complexity value above the 99.5th percentile ( $> 17,000$  bytes). In this frame EMU PD J205842.8-573658 (labelled ORC2) in the top right is the dominant source. This frame also contains EMU PD J205856.0-573655 (labelled ORC3).

Number of Evaluations	Percentage of samples
1	0.0%
2	0.2%
3	0.9%
4	5.2%
5	12.4%
6	23.7%
7	24.3%
8	18.6%
9	10.5%
10	3.5%
11	0.6%
12	0.1%

**Table 3.** Distribution of evaluation counts across the zoo sample

Zoo label	Average number of votes	Average consensus
Anomalous	6.8	70%
Complex	6.9	77%
Simple	6.9	87%
No source	6.5	78%
No consensus	6.4	48%

**Table 4.** Average number of evaluations and consensus level across the outcome labels

### 5.3 Performance evaluation

#### 5.3.1 Completeness and Purity

To measure completeness and purity using the results from the Anomaly Zoo, we use the following metrics:

$$\text{Completeness} = \frac{TP}{TP + FN}. \quad (7)$$

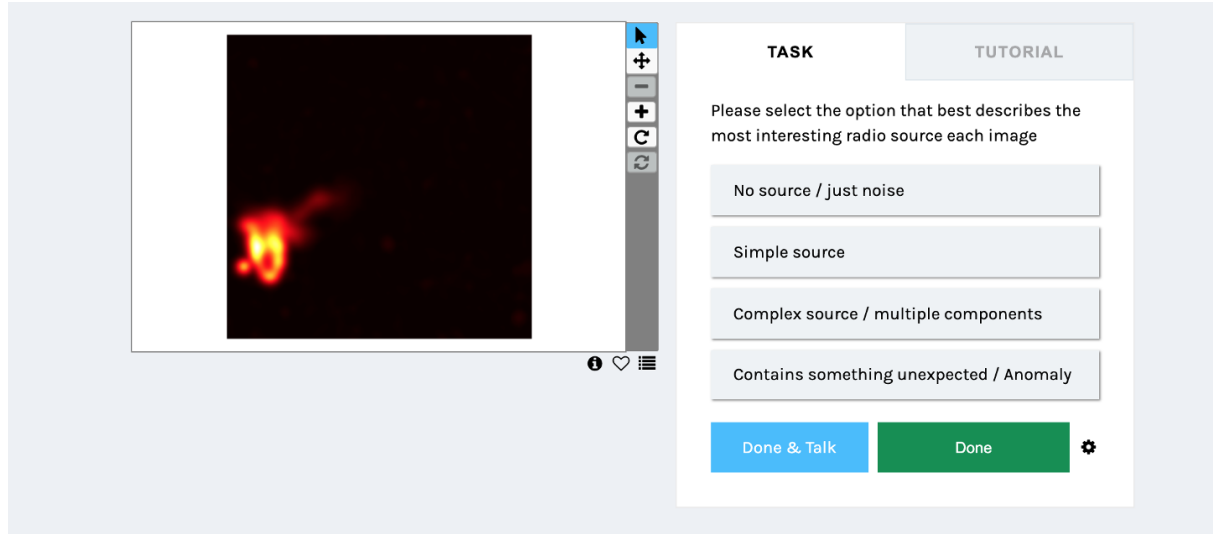


**Figure 8.** Example workflow from Anomaly in the EMU Zoo. In this example we pick a frame containing 2MASX J21291901-5053040, bent tail radio galaxy near ABELL 3771 cluster.

Classification	Count: Non-bias sample (n=1528)	Count: Enrichment (n=99)	Count: Combined Sample (n=1627)
Anomalous	7	17	24
Complex	366	57	423
Simple	1059	12	1071
No source	31	0	31
No consensus	65	13	78

**Table 5.** Classification counts by consensus for each of the options provided in the EMU-PS Anomaly in the EMU Zoo. The enrichment sample supplements the zoo sub-sample with frames measuring complexity above the 99.5th percentile. This creates a bias for the purpose of calculating completeness but improves the sample size for calculation of purity above prospective partition thresholds. This data shows that 86% of the enrichment sample, where consensus was reached, contains frames classified as containing complex and anomalous sources.

$$\text{Purity} = \frac{TP}{TP + FP}, \quad (8)$$

Here FP are False Positives (or Type I errors, objects misidentified as being of interest), FN are False Negatives (or Type II errors, complex and unusual objects misidentified as being simple), TP are True Positives (correct positive classifications) and TN are True Negatives (correct negative classifications).

Purity (also commonly referred to as precision) determines the number of correct positive classifications as a fraction of all positive classifications,  $TP/(TP+FP)$ , while completeness (also commonly referred to as recall) determines the number of correct positive classifications as a fraction of the total number of real positives ( $RP=TP+FN$ ), and so is  $TP/RP$ . The fraction of positive objects that have been missed would be  $1 - \text{completeness}$ , in the binary classification case.

### 5.3.2 Informedness

An alternative framework for measuring performance involves the use of Receiver Operating Characteristic (ROC) curves. The use of ROC curves to construct a comparative framework has been adopted in the machine learning literature (Fürnkranz & Flach 2005). These approaches account for chance level performance and can also be used to account for the cost weightings of negative and positive cases. ROC analysis examines the false positive rate (FP/RN) versus the true positive rate (TP/RP), which can be used to account for the trade-off between these two measures.

The maximum positive distance of the receiver operating characteristic (ROC) curve from the 45 degree chance line is known as Youden's J statistic (Youden 1950) or as the Informedness measure (Powers 2011). The Informedness measure is equivalent to the subtraction of the false positive rate (FPR) from the true positive rate (TPR) as follows:

$$\text{Informedness} = \frac{TP}{TP + FN} - \frac{FP}{TN + FP} = TPR - FPR \quad (9)$$

Powers (2011) shows that Informedness is an unbiased estimator of above chance performance. The measure incorporates both Type I errors (False Positives) and Type II errors (False Negatives) and describes the improved performance of the measured classifier with respect to chance, costing true positives and false positives in a way analogous to how a bookmaker fairly prices the odds (Powers 2011). For this reason the measure is also referred to as Bookmaker Informedness. The Informedness measure is defined on a  $(-1,1)$  interval and gives equal weighting to the true positive and false positive rate.

Informedness appears appropriate for evaluating the effectiveness of alternative approaches at detecting and classifying complex and unusual observations in large astronomical data. The Informedness measure relates to the following objectives of classification:

- (i) **Maximise true positive rate** (i.e. minimise the type II error rate) - ensuring the search space contains as many truly interesting things as possible.
- (ii) **Minimise false positive rate** (i.e. minimise the type I error

rate) - ensuring the search space does not become too large and predominantly contains truly interesting things.

Removing false positives reduces the search space, and the associated costs of handling larger data, helping to make the discovery process more efficient. Due to the likely small number of actually unusual observations (new types of objects) compared to normal observations (objects belonging to an already known or common class) in the total sample, the metric is likely to be more sensitive to small changes in the true positive count resulting from misclassification or disagreement between zoo volunteers.

In assessing the effectiveness of the approach, a key consideration is the reduction of the type II error rate, measuring the effectiveness of the approach at identifying as many of the unusual observations as possible. Minimising the type I error rate is also of importance in providing a significant reduction in the search space. Reducing the type I error rate also reduces contamination of the search space by simple sources and noise. This is reflected in the complementary measure of purity. For these reasons the Informedness and Purity measures were chosen as the principle criteria for evaluating the partition boundary.

#### 5.4 Sub-sampling of EMU-PS frames

Selecting sample frames from the EMU-PS scan to be evaluated by the zoo was done in two phases. The first phase involved blind unbiased sub-sampling ( $n=1528$ ) by sampling proportionally across the distribution of complexity values. Sampling was performed on non-overlapping frames (using the first occurrence) without replacement. The second phase involved enrichment sampling ( $n=99$ ) from a EMU-PS scan done at a stride length of 32 pixels, half the original stride length. The reduced stride length samples from the EMU-PS more thoroughly, and so can capture frames of higher complexity than the scan done at a stride length of 64 pixels, extending the tail of high-complexity values. Due to the much larger number of frames produced ( $n = 1.4$  million) when using the smaller stride length, only frames above the 99.5th percentile complexity value were retained as part of the sample ( $n = 7,000$ ). Sub-sampling was performed uniformly across this tail to produce the enrichment sample ( $n=99$ ).

The purpose of the enrichment sample was to supplement the tail of the 64 pixel stride sub-sample distribution with frames of complexity above the 99.5th percentile. The sample size for the zoo was limited ( $n=1627$ ) to ensure all frames could be evaluated by a larger number of volunteers, however this results in poor sub-sampling from the far right (high complexity) tail. The enrichment sample was intended to provide better representation of the type of observations found within frames beyond the 99.5th percentile. Classification counts for each of the zoo classes are shown in table 5. The enriched tail is shown in the comparative histograms in figure 9.

The first phase of sampling allowed the completeness (also referred to as recall) to be assessed at a given complexity threshold. The enrichment sample creates a bias for the purpose of calculating completeness by over-representing high complexity objects in the total zoo sample and accordingly was not included in the non-bias sample used to assess completeness.

The second phase, enrichment sampling, was performed to increase the sample size of unusual observations and provide a more thorough evaluation of the purity. The purity measurements both before and after the inclusion of the enrichment sample are shown in table 7 while the anomaly counts both before and after are shown in table 5.

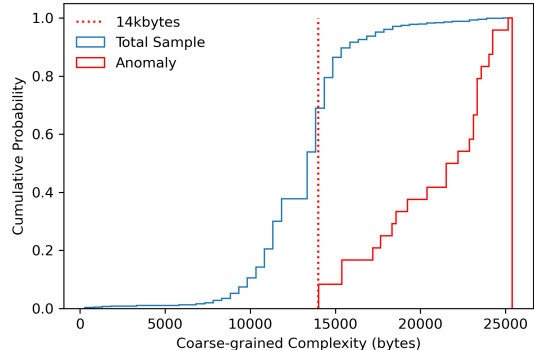


**Figure 9.** Cumulative probability of complexity values from both the Total sample and for anomalies identified in the zoo

Table 5 shows that 86% of the enrichment sample, where consensus was reached, contains frames classified as containing complex and anomalous objects. This is consistent with the purity of 85% measured above a complexity value of 17,000 bytes across the combined sample, including enrichment, as shown in table 6.

Figure 10 shows the histogram of complexity values from the zoo sub-sample. Complexity values ranging from 12,200 bytes to 13,400 bytes were not included in the zoo sub-sample due to the selection procedure of inward sampling from the tails. Values within this range occur within the inner quartiles of the EMU-PS sample. The zoo results, as depicted in figure 9, show that all sources classified by zoo participants as unexpected or anomalous have a measured complexity value of approximately 14,000 bytes or greater. It is assumed that the frames not sub-sampled within the complexity range 12,200 bytes to 13,400 bytes would have minimal impact on the assessment of completeness, given the low probability of sources being classified as unexpected or anomalous below 14,000 bytes. Any false negatives (Type II errors) resulting from defining the partition boundary at this level or above are expected to be few. This is supported by the large zoo sub-sample below 14,000 bytes, over 60% of the total zoo sub-sample, in which no sources were classified as anomalous. Furthermore the fraction of anomalous sources appears to reduce quickly at lower complexity values, as demonstrated by the steep slope at high complexity values in the cumulative probability distribution for anomalies, as shown in figure 9. Accordingly, re-sampling from within the missing range was not deemed as necessary.

#### 5.5 Measuring the effectiveness of partitions

We evaluate the partition boundary using a binary classification approach, evaluating both the purity and completeness of the anomaly catalogue. When evaluating completeness we consider the positive class to include only frames containing something unexpected or anomalous and the negative class to include all other frames. Limiting the positive class to only frames containing unexpected or anomalous sources provides a measurement framework that will assist in defining an anomaly catalogue with the objective of supporting new and novel scientific discoveries in an efficient manner. A catalogue containing all extended sources would be much larger and would increase the search space for novel and anomalous objects, making the discovery process less efficient.

When evaluating purity we count within the positive class both frames containing something unexpected or anomalous as well as

EMU-PS Anomaly in the EMU Zoo sub-sample excluding enrichment sample (n=1528)				
Partition boundary	Completeness (Anomalous only)	False Positive Rate (Anomalous only)	Informedness (Anomalous only)	Purity (Complex and Anomalous)
Complexity $\geq 14,000$ bytes	1.00	0.37	0.63	0.43
Complexity $\geq 14,000$ bytes, SNR $\geq 0.14$	1.00	0.17	0.83	0.56
EMU-PS Anomaly in the EMU Zoo sub-sample including enrichment sample (n=1627)				
Complexity $\geq 17,000$ bytes	0.83	0.06	0.78	0.85

**Table 6.** Informedness and purity measures at various partition boundaries

EMU-PS Anomaly in the EMU Zoo sub-sample excluding enrichment sample (n=1528)				
Partition boundary	Completeness (Anomalous only)	False Positive Rate (Anomalous only)	Informedness (Anomalous only)	Purity (Complex and Anomalous)
Catalogue Boundary (functional form)	0.86	0.04	0.82	0.57
Catalogue Boundary + Complexity $\geq 15,000$ bytes	0.71	0.02	0.69	0.76
Catalogue Boundary + Complexity $\geq 17,000$ bytes	0.43	0.01	0.42	0.81
EMU-PS Anomaly in the EMU Zoo sub-sample including enrichment sample (n=1627)				
Catalogue Boundary (functional form)	0.96	0.06	0.90	0.75
Catalogue Boundary + Complexity $\geq 15,000$ bytes	0.92	0.04	0.88	0.88
Catalogue Boundary + Complexity $\geq 17,000$ bytes	0.83	0.02	0.81	0.94

**Table 7.** Informedness and purity measures at various partition boundaries. The functional form of the complexity boundary is given by equation 10, and plotted in figure 11.

Catalogues created					
Name	Boundary	Size	Percentage of scan retained	Completeness (non-bias)	Purity (Enriched)
Most complete	Complexity boundary (function)	n= 16,157	5%	0.86	0.75
Compromise	Complexity boundary + Complexity $\geq 15,000$ bytes	n= 3,791	1%	0.71	0.88
Most pure	Complexity boundary + Complexity $\geq 17,000$ bytes	n= 1,854	0.5%	0.43	0.94

**Table 8.** Informedness and purity measures for different anomaly catalogues. The functional form of the complexity boundary is given by equation 10, and plotted in figure 11.

frames containing at least one complex source or a source with multiple components. The negative class then includes frames containing simple sources and no sources. The use of a broader definition for the positive class when measuring purity reflects the low frequency of sources deemed by consensus as being anomalous and the potential overlap in complexity values of frames evaluated as containing complex and anomalous objects. This helps ensure that when optimising partitions in terms of purity, completeness is preserved with respect to anomalous sources. Contamination by complex sources is deemed acceptable as these sources will still be interesting to some observers and are not deemed harmful if the overall catalogue size is small enough to support an efficient search for novel discoveries as achieved through maximising the informedness.

### 5.5.1 Complexity boundaries

Figure 11 shows both the coarse-grained complexity and the signal-to-noise ratio (SNR), and the relationship between them, for the

EMU-PS zoo sub-sample inclusive of the enrichment sample (n=1627). The SNR is calculated as the reciprocal of the coefficient of variation for the channel intensity values. As frames contain predominantly channel values close to zero, these ratios are typically well below unity. The rationale for adopting this metric is discussed further in section 5.6. The figure also shows the classification of frames derived through consensus from EMU in the Anomaly Zoo. We see that frames evaluated as containing an anomalous object by consensus are measured as having larger coarse-grained complexity and SNR values, with all anomalous objects having complexity values greater than 14,000 bytes and an SNR ratio greater than 0.14. The figure also shows that the concentration of frames with complex and anomalous zoo labels increases in the tail above the 99.5th percentile, a complexity value of approximately 17,000 bytes.

Table 6 shows that completeness in the zoo sub-sample above a complexity threshold of 14,000 bytes is 1.00, equivalent to 100% retention of anomalous objects, however the false positive rate of 0.37 results in an informedness of 0.63. The false positive rate here is measured based on the proportion of frames not containing anomalous objects by consensus that fall above the threshold. The

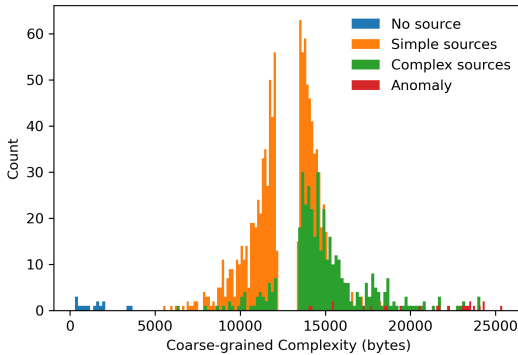


**Figure 10.** Histogram partitioned by consensus votes from the zoo. Bins in the range 12,200 bytes to 13,400 bytes were omitted as described in section 5.4.

results show that when an SNR threshold of 0.14 is incorporated, the completeness remains at 1.00, however the false positive rate reduces to 0.17 resulting in an informedness of 0.83.

In order to segment frames containing anomalous sources, and reduce the false positive rate, we fit (based on visual inspection) a function as the catalogue boundary in terms of the complexity  $C(f(x))$  and SNR. This is illustrated in Fig. 11 as an exponential curve where truth labels were defined using consensus votes from zoo classifications. The functional catalogue boundary can also be expressed in terms of a log ratio adjustment of a lower bound complexity value for anomalous frames

$$C(f(x)) \geq 13101 \ln \left( \frac{2}{\sqrt[3]{\text{SNR}}} \right), \quad (10)$$

To be considered a candidate for the anomaly catalogue, a frame must have a complexity value greater than the right side of Eqn. 10. This equation provides a complexity boundary of  $C(f(x)) > 14000$  when the SNR of the frame is roughly 0.3. The majority of frames have a SNR less than 0.3 (as we can see from Fig. 11), and so would require a higher complexity to be considered as part of the anomaly catalogue. We propose that a similar partition will be effective with respect to the full EMU survey

Table 7 shows that this function based catalogue boundary provides a completeness of 0.86, an informedness of 0.82, and a purity of 0.57. The informedness and purity of the function based catalogue boundary are comparable to the orthogonal thresholds, made at a complexity of 14,000 bytes and SNR at 0.14 as shown in table 6. A key advantage of the function based catalogue boundary however is the much smaller false positive rate with respect to anomalies, approximately one third ( $\sim 33\%$ ) the size. This results in a much more efficient search space for unusual objects and can be used to produce an anomaly catalogue of a more manageable size. Imposing stricter complexity thresholds on the catalogue boundary can further reduce the false positive rate and improve the purity as shown in table 7. Results including the enrichment sample suggest that a significant improvement in purity can be achieved when stricter complexity thresholds are applied, with results showing a purity of 0.88 and 0.94 when applying complexity thresholds of 15,000 bytes and 17,000 bytes respectively. These results allow the trade-off between catalogue size, completeness and purity to be evaluated for different catalogue boundary choices. We use estimates of completeness based on the non-bias sub-sample to provide more accurate estimates by avoiding the allocation of too much weight

to the tail through oversampling. Conversely, we use estimates of purity based on the enriched sub-sample to provide a better representation of the concentration of complex and anomalous sources above the selected complexity cuts.

### 5.5.2 Anomaly Catalogues

We construct three anomaly catalogues, as shown in Table 8, the first based only on a function incorporating complexity and SNR values to formulate the boundary, and the other two combining the function based catalogue boundary with a complexity cut at  $\geq 15,000$  bytes and  $\geq 17,000$  bytes. Using a function based catalogue boundary that incorporates both complexity and the SNR, as expressed by Eqn. 10, maximises the informedness of the catalogue sample, as shown in table 7, by reducing the retention of false positives.

Using the function based catalogue boundary, without any further complexity cuts, provides the highest completeness of 0.86. However, it also produces a very large catalogue of  $n=16,157$  frames with an estimated purity of 0.75.

To provide a more efficient search space, that promotes the discovery of unusual and novel objects, we introduce further complexity cuts to reduce the catalogue size and increase the purity. At a complexity cut of  $\geq 17,000$  bytes, the catalogue size is reduced significantly from 16,157 frames to 1,854 frames with an estimated purity of 0.94 where the positive class includes only anomalous and multiple components sources. This suggests that 94% of objects in this catalogue will have some structure, and will be more interesting than simple unresolved sources or single component sources. We expect that very few of the frames belonging to this catalogue would be classified as containing only simple objects or noise. This is the smallest catalogue, and provides a fast search space, minimising the number of false positives, however the low completeness of 0.43 presents a significant risk that some new and interesting objects of interest will not be captured.

At a compromise complexity cut of  $\geq 15,000$  bytes, the catalogue size of  $n=3,791$  remains significantly smaller than the catalogue when excluding a complexity cut ( $n=16,157$ ). The estimated purity of 0.88 and completeness of 0.71 also provide a middle ground, combining improved coverage of anomalies with a high concentration of interesting objects, both complex and anomalous. We include examples of interesting frames from this catalogue in Appendix A. The full catalogues are also available by contacting the author.

## 5.6 Classification errors

The evaluation of classification errors provides important context for selecting a partition boundary for an anomaly catalogue. Type II errors, representing the incorrect classifications of true positives (i.e. false negatives), remained low at the boundaries evaluated. All anomalies identified by zoo participants were contained by orthogonal thresholds, made at a complexity of 14,000 bytes and an SNR of 0.14. The function based catalogue boundary produced only one false negative as shown in figure 11 (below the perforated exponential line).

False negative errors may arise due to the removal of meaningful information by the smoothing functions, potentially due to the sparse or faint representation of complex features, discernible to the human eye or through additional measurements, but having a reduced impact on the information content of the frame itself. This was the case with the single false negative falling outside of the

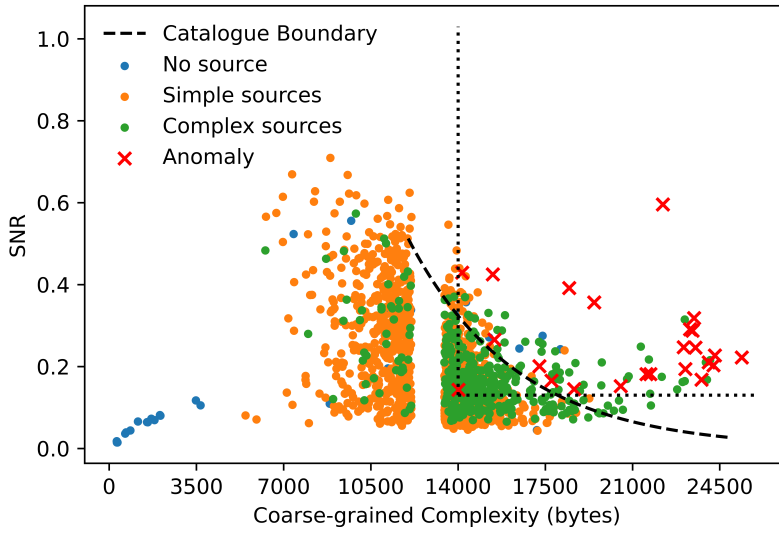


**Figure 11.** Scatter plot showing the coarse-grained complexity and the signal-to-noise ratio (SNR), and the relationship between them, for the EMU-PS zoo sub-sample inclusive of the enrichment sample ( $n=1627$ ). The figure shows the classification of frames derived through consensus from the zoo (Anomaly in the EMU Zoo) and the function based catalogue boundary for anomalies (Catalogue Boundary) shown in its exponential form in this figure and expressed in terms of a log ratio adjustment of a lower bound complexity value in equation 10.

function based catalogue boundary. This example is illustrated in figure 12, where a faint complex structure is apparent in the top left corner of the frame. While consensus converged on the classification of this frame as an anomaly, 3 out of 7 zoo participants considered the frame as not containing any complex structures, and evaluated the frame as containing only simple objects (most likely referring to the bright source at the bottom of the frame towards the right side). Even though this frame falls outside of the function based catalogue boundary, a complexity value of over 14,000 bytes suggests that this frame does contain a complex structure. In alternative frames, outside of the zoo sub-sample, even larger complexity values are attributed to this structure. Further investigation shows that the faint complex radio emission in the top left corner of the frame appears to be due to a face-on spiral galaxy ESO 236-G008 ( $z=0.03088$ , optical angular diameter  $1.5'$ ). Interestingly, the complexity value separates this frame from even more unusual faint radio structures such as ORC-like ringed radio emissions.

False negative errors may also be due to mislabelling of noise and simple objects as positives (i.e. incorrect assignment of truth labels) due to the judgement error of zoo participants. Errors may also be due to a failure of zoo participant evaluations to converge accurately due to the small number of volunteers involved in this study with the appropriate expertise to evaluate certain objects, given consensus is based on five evaluations or greater.

Type I errors, representing the incorrect identification of simple sources as complex (i.e. false positives), may be due to the presence of non-random information deemed by a human observer to be incidental and not contributing to the complexity of the source itself. An example could be a telescope imaging artefact containing structure, such as a point spread function originating from a brighter source. Type I errors may also occur where multiple simple sources are captured within a frame, as the number of sources captured in each frame can vary significantly.

Errors again may also be due to a failure of volunteer evaluations to converge on accurate truth labels, in this case mislabelling

frames containing complex and unusual objects as negatives potentially due to the loss of information in each frame due to the sampling process. This is particularly likely where only part of an interesting source was captured in the sample frame. For example, the X-shaped radio galaxy 2MASX J20180125-5539312, as shown in figure 13, is large enough such that the scan frames capture only part of this larger structure. These examples were often misclassified by participants as frames containing only noise or simple objects. However, expert astronomers did in fact identify these frames as containing complex and anomalous structures, even though misclassifications by other volunteers resulted in the failure of some of these frames to have consensus votes that converge on a positive label. Furthermore, the human criteria for what is interesting or anomalous may be somewhat tarnished by previous exposure and not judged on its own merits (e.g. a galaxy image may have a high complexity, but be identical to images previously seen by the human judge and accordingly classified as simple).

Alternatively, type I errors may be explained by the retention of random inputs not removed by the smoothing function. In S19 we demonstrated that in the ATLAS sample there was a large amount of noise in the simple sources at baseline. This presents a risk that in some images random inputs will take the form of incidental structure that may not be removed as smoothing increases. Where random inputs are retained after smoothing, segmentation efficiency is likely to be improved by incorporating thresholds in both the coarse-grained complexity and the SNR, as incidental structure and imaging artefacts are less likely to have the same gradient structure as astronomical sources and are therefore likely to be distributed more uniformly across the available channel values. Figure 11 illustrates the benefit of incorporating the SNR to reduce false positives (type I errors).

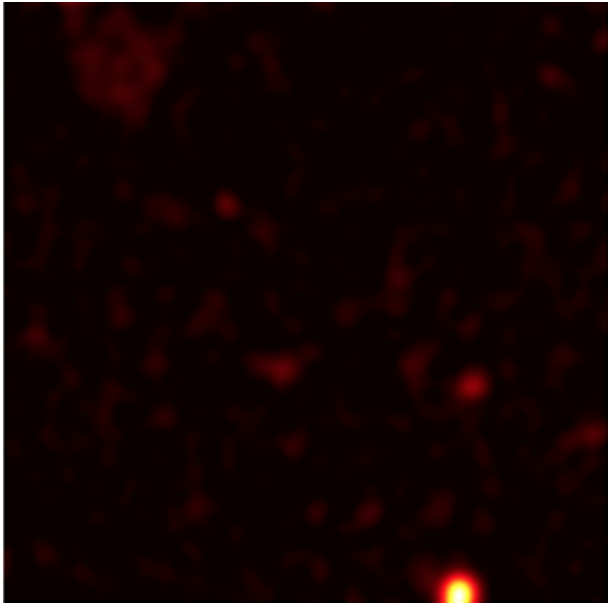


**Figure 12.** False negative errors may arise due to the removal of meaningful information by the smoothing functions due to the faint representation of complex features. This was the case with the single false negative falling outside of the function based catalogue boundary. A faint complex structure is apparent in the top left corner of the frame. While consensus converged on the classification of this frame as an anomaly, 3 out of 7 zoo participants evaluated the frame as containing only simple objects (most likely referring to the bright source at the bottom of the frame towards the right side). In alternative overlapping frames, outside of the zoo sub-sample, even larger complexity values are attributed to this structure. Further investigation shows that the faint complex radio emission in the top left corner of the frame appears to be due to a face-on spiral galaxy ESO 236-G008 ( $z=0.03088$ , optical angular diameter  $1.5'$ ). Interestingly, the complexity value separates this frame from even more unusual faint radio structures such as ORC-like ringed radio emissions.

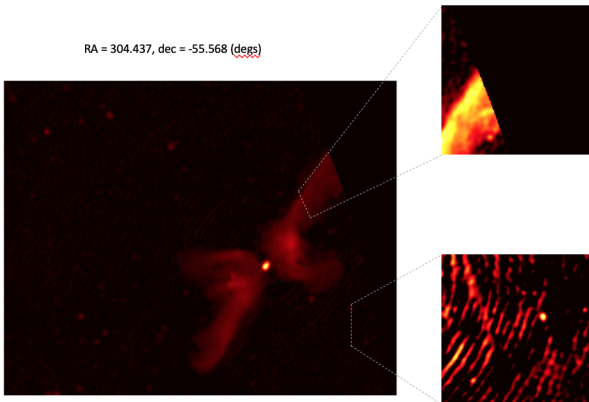


**Figure 13.** The X-shaped radio galaxy 2MASX J20180125-5539312 provides an example where frames captured only part of the larger structure. These partial frames were sometimes misclassified by participants as not being of interest.

## 6 CONCLUSION

- The coarse-grained complexity can be used as a tool for identifying unusual and complex images, useful for segmenting complex images from simple images, as demonstrated in S19. In this work we apply it to new data to identify and segment unusual sources (i.e. anomalies).

- We extend the method used in S19 and develop a new approach for measuring the coarse-grained complexity based on an autoencoder. The size in bits of the source encoding segment of the latent space can be used as a coarse-grained complexity measure, while the size of the noise segment can be interpreted as a measure of the noise level. While the autoencoder provides theoretical benefits (e.g. training for invariance to rotation) results show comparable performance to the approach implemented in S19 (using `gzip`), with both approaches proving effective.

- We scanned the mosaic image of Pilot Survey of the Evolutionary Map of the Universe, measuring the complexity of frames rather than individual sources, and examined the distribution of complexity values. An important feature of the scan method is that the frames are sampled from the EMU-PS data in a blind manner, without reference to any source catalogue.

- We found that the high-value tail of the complexity distribution comprises many unusual, complex and extended objects. Extended sources featured heavily in the tail above the 95th percentile, with wide angle tail radio galaxies and objects of a more anomalous appearance were apparent from above the 99th percentile. The ability of the coarse-grained complexity measure to segment these sources in the distribution tail shows the effectiveness of this approach at identifying scientifically interesting observations in large data sets in an efficient manner.

- Our results demonstrate the effectiveness of this approach in recovering known extended or complex structures.

- We use a Zooinverse project to produce crowd-sourced labels for a sub-sample of frames produced by a blind scan of the EMU-PS data to evaluate the effectiveness of the coarse-grained complexity as an anomaly partition. We identify an effective anomaly partition using the coarse-grained complexity and SNR values, that can be used to generate an anomaly catalogue and propose that a similar partition will be effective with respect to the full EMU survey.

- We generate three anomaly catalogues using coarse-grained complexity and SNR values to partition the frames. The most complete catalogue uses a function based on complexity and SNR values to formulate the boundary, and has  $n=16,157$  frames, less than 5% of the total  $n=365,000$  frames produced from the EMU-PS scan, with an estimated completeness of 0.86 and a purity of 0.75. The most pure catalogue has an additional complexity cut at  $\geq 17,000$  bytes (on top of the functional boundary), with a catalogue size of 1,854 frames and an estimated purity of 0.94. The compromise catalogue uses a lower complexity cut of only  $\geq 15,000$  bytes and has a catalogue size of  $n=3,791$ , with a purity of 0.88 and completeness of 0.71, providing a middle ground with respect to catalogue size and completeness. We make these catalogues available to the community.

The analysis has demonstrated the ability of the coarse-grained complexity to single out regions of the sky that contain complex and unusual sources, in a manner that can be computed at worst-case linear time complexity without reference to the ensemble or existing catalogue data. This will be an efficient and powerful tool in identifying anomalous sources in the full EMU survey, as well as subsequent large and deep radio continuum and optical imaging surveys.

## ACKNOWLEDGEMENTS

We thank all the members of the radio astronomy community who provided their time and expertise in classifying the images as part of the Anomaly in the EMU Zoo Zooniverse.org project. DP is supported by the project 우주거대구조를 이용한 암흑우주 연구 (“Understanding Dark Universe Using Large Scale Structure of the Universe”), funded by the South Korean Ministry of Science. ELA gratefully acknowledges support from the UK Alan Turing Institute under grant reference EP/V030302/1 and from the UK Science & Technology Facilities Council (STFC) under grant reference ST/P000649/1. H.A. benefited from grant CIIC 138/2022 of DAIP, Universidad de Guanajuato, Mexico. HT gratefully acknowledges the support from the Shuimu Tsinghua Scholar Program of Tsinghua University. JP acknowledges support from the Science and Technology Facilities Council (STFC) via grant ST/V000624/1.

The Australian SKA Pathfinder is part of the Australia Telescope National Facility (<https://ror.org/05qajvd42>) which is managed by CSIRO. Operation of ASKAP is funded by the Australian Government with support from the National Collaborative Research Infrastructure Strategy. ASKAP uses the resources of the Pawsey Supercomputing Centre. Establishment of ASKAP, the Murchison Radio-astronomy Observatory and the Pawsey Supercomputing Centre are initiatives of the Australian Government, with support from the Government of Western Australia and the Science and Industry Endowment Fund. We acknowledge the Wajarri Yamatji people as the traditional owners of the Observatory site.

This publication uses data generated via the Zooniverse.org platform, development of which is funded by generous support, including a Global Impact Award from Google, and by a grant from the Alfred P. Sloan Foundation.

## DATA AVAILABILITY

The EMU Pilot Survey radio continuum stokes I image used in this analysis described in section 3 was generated from data available from the CSIRO ASKAP Science Data Archive (CASDA). The anomaly catalogues generated as part of this study are available by contacting the author.

## REFERENCES

Aaronson S., Carroll S., Ouellette L., 2014, <http://arxiv.org/abs/1405.6903v1>

Aniyan A. K., Thorat K., 2017, *ApJS*, 230, 20

Chaitin G., 1975, *J. Assoc. Comput. Mach.* 22, 329–340

Chaitin G., Arslanov A., Calude C., 1995, CDMTCS Research Report Series CDMTCS-008

Charnock T., Moss A., 2017, *ApJ*, 837, L28

Cheng T.-Y., Huertas-Company M., Conselice C. J., Aragon-Salamanca A., Robertson B. E., Ramachandra N., 2021, *MNRAS*, 503, 4446

DESI Collaboration et al., 2016, arXiv e-prints, [p. arXiv:1611.00036](https://arxiv.org/abs/1611.00036)

Dewdney P. E., Hall P. J., Schilizzi R. T., Lazio T. J. L. W., 2009, *IEEE Proceedings*, 97, 1482

Dieleman S., Willett K., Dambre J., 2015, *MNRAS*, 450, 1441–1459

Doré O., et al., 2014, arXiv e-prints, [p. arXiv:1412.4872](https://arxiv.org/abs/1412.4872)

Franzen T. M. O., et al., 2015, *MNRAS*, 453, 4020

Fürnkranz J., Flach P., 2005, *Mach Learn*, 58, 39–77

Gabbard H., Messenger C., Heng I. S., Tonolini F., Murray-Smith R., 2022, *Nature Physics*, 18, 112

Galvin T. J., et al., 2020, *MNRAS*, 497, 2730

Gell-Mann M., 1994, *The Quark and the Jaguar: Adventures in the Simple and the Complex..* Henry Holt and Company

Giles D. K., Walkowicz L., 2020, *MNRAS*, 499, 524

Gupta N., Huynh M., Norris R. P., Wang R., Hopkins A. M., Andernach H., Koribalski B. S., Galvin T. J., 2022, In Preparation

Huertas-Company M., et al., 2015, *ApJS*, 221

Ivezic Ž., et al., 2019, *ApJ*, 873, 111

Karpenka N. V., Feroz F., Hobson M. P., 2013, *MNRAS*, 429, 1278

Kessler R., et al., 2010, *PASP*, 122, 1415

Kim D.-W., Bailer-Jones C. A. L., 2016, *A&A*, 587, A18

Koribalski B. S., Norris R. P., Andernach H., Rudnick L., Shabala S., Filipović M., Lenc E., 2021, *MNRAS*, 505, L11

Levine J., 2012, Technical Report RFC 6713, The ‘application/zlib’ and ‘application/gzip’ Media Types, [doi:10.17487/RFC6713](https://doi.org/10.17487/RFC6713).

Li M., Vitanyi P., 2008, *An Introduction to Kolmogorov Complexity and Its Applications*. Springer, 3rd. ed.

Lochner M., Bassett B. A., 2021, *Astronomy and Computing*, 36, 100481

Lochner M., McEwen J. D., Peiris H. V., Lahav O., Winter M. K., 2016, *The Astrophysical Journal Supplement Series*, 225, 31

Lukic V., Brüggen M., Banfield J. K., Wong O., Rudnick L., Norris R. P., Simmons B., 2018, *MNRAS*, 476, 246

Lukic V., Brüggen M., Mingo B., Croston J. H., Kasieczka G., Best P., 2019, *MNRAS*, 487, 1729

Ma Z., Zhu J., Li W., Xu H., 2018, in 2018 14th IEEE International Conference on Signal Processing (ICSP). pp 522–526

Middleberg E., et al., 2008, *AJ*, 135, 1276

Mostert R. I., et al., 2021, *Astronomy & Astrophysics*, 645, A89

Nishikawa-Toomey M., Smith L., Gal Y., 2020, arXiv preprint [arXiv:2011.08714](https://arxiv.org/abs/2011.08714)

Norris R. P., 2017, *Publ. Astron. Soc. Australia*, 34, e007

Norris R. P., et al., 2006, *AJ*, 132, 2409

Norris R. P., et al., 2011, *Publ. Astron. Soc. Australia*, 28, 215

Norris R. P., et al., 2021a, *Publ. Astron. Soc. Australia*, 38, e003

Norris R. P., et al., 2021b, *Publ. Astron. Soc. Australia*, 38, e046

Norris R. P., et al., 2022, *MNRAS*, 513, 1300

Otrupcek R. E., Wright A. E., 1991, *PASA*, 170

Polsterer K. L., Gieseke F., Doser B., 2019, *Astrophysics Source Code Library*, pp ascl-1910

Portillo S. K., Parejko J. K., Vergara J. R., Connolly A. J., 2020, *AJ*, 160, 45

Powers D. M., 2011, *Journal International Journal of Machine Learning Technology*, 2, 37

Ralph N. O., et al., 2019, *PASP*, 131, 108011

Robinson B. J., 1987, *Publ. Astron. Soc. Australia*, 7, 220

Segal G., Parkinson D., Norris R. P., Swan J., 2019, *PASP*, 131, 108007

Shimwell T. W., et al., 2017, *A&A*, 598, A104

Shimwell T. W., et al., 2022, *A&A*, 659, A1

Vafaei Sadr A., Bassett B. A., Kunz M., 2021, *Neural Computing and Applications*, pp 1–11

Whiting M., Voronkov M., Mitchell D., Askap Team 2017, in Lorente N. P. F., Shortridge K., Wayth R., eds, *Astronomical Society of the Pacific Conference Series Vol. 512, Astronomical Data Analysis Software and Systems XXV*. p. 431

Wu C., et al., 2019, *MNRAS*, 482, 1211

Youden W. J., 1950, *Cancer*, 3, 32

Zenil H., Delahaye J.-P., Gaucherel C., 2012, *Complexity*, 17, 26

## APPENDIX A: COMPLEXITY CATALOGUES

Table A1 outlines three anomaly catalogues produced using various complexity cuts that are available by contacting the author. Summary statistics are detailed in Table 8.

Examples of interesting non-overlapping frames from the catalogue, with a complexity of 17,000 bytes or greater, are shown in figure A1. Frames with figure reference 2C, 4A, 4B, 4C and 7A were found efficiently within the catalogue search space. The remaining frames shown in figure A1 were sampled from within

Catalogues created		
Catalogue	Size	Location
Catalogue Boundary (functional)	n= 16,157	Please email the author
Catalogue Boundary, Complexity $\geq$ 15,000 bytes	n= 3,091	as above
Catalogue Boundary, Complexity $\geq$ 17,000 bytes	n= 1,224	as above

**Table A1.** Locations of anomaly catalogues

Reference	RA (deg)	Dec (deg)	complexity (bytes)	> Percentile	Comments
1a	306.9070	-55.3286	17348	> 99.5	DES J202714.57-551846.9 FR-II
1b	319.1032	-63.0100	18932	> 99.9	DES J211634.20-630107.1 FR-I wide angle tail (WAT)
1c	325.9677	-48.3775	19749	> 99.9	2MASX J21440210-4818581 FR-II
1d	324.1762	-54.5852	19670	> 99.9	NGC 7090 edge-on spiral
2a	306.7129	-55.3512	18965	> 99.9	DES J202644.45-552227.3 FR-II
2b	323.8758	-62.1123	19467	> 99.9	2MASX J21351149-6204432 FR-I, Fairall 106: optical shells
2c	322.3302	-50.8773	19316	> 99.9	2MASX J21291901-5053040 FR-I, bent tail radio galaxy near ABELL 3771 cluster
2d	325.8048	-61.4724	19476	> 99.9	2MASX J21431182-6128184 FR-I
3a	330.2012	-56.2027	19023	> 99.9	EMU-PS J220026.3-561030, circular morphology
3b	324.9420	-51.3488	17367	> 99.5	2MASX J21392989-5123440 FRI, WAT
3c	309.0821	-57.6315	19987	> 99.9	ESO 143-G035, Fairall 74 peculiar bent tail
3d	327.8800	-55.2066	19152	> 99.9	2MASX J21512991-5520124 FR-I, WAT
4a	304.7219	-55.7009	19839	> 99.9	X-shaped radio source PKS 2014-55 (2MASX J20180125-5539312)
4b	304.365	-55.5981	19745	> 99.9	
4c	314.6710	-57.5859	17570	> 99.5	the dominate source is EMU PD J205842.8-573658 (ORC2) and frame also contains EMU P
4d	335.2956	-50.3287	19629	> 99.9	2MASX J22212664-5016453 FR-I, WA and DES J222105.94-501825.2 FR-II X-shaped
5a	327.3157	-60.6941	18870	> 99.9	NGC 7125 face-on spiral galaxy
5b	308.6064	-52.9265	17992	> 99.8	DES J203408.30-525341.8 FR-II
5c	325.9255	-51.1071	17212	> 99.5	DES J214331.34-510541.1, peculiar arcs in lobes
5d	334.1724	-62.8608	17867	> 99.8	DES J221640.02-625241.6 FR-II
6a	330.7123	-51.3059	17419	> 99.6	ESO 237-G027 irregular blue galaxy
6b	314.4684	-51.8156	17655	> 99.7	NGC 6984 spiral galaxy
6c	324.5476	-59.6211	17411	> 99.6	DES J213808.45-593718.4 FR-II X-shaped
6d	311.4731	-51.0829	20230	> 99.9	2MASX J20455226-5106267 FR-I, WAT
7a	323.5376	-53.6292	20179	> 99.9	PKS 2130-538 / EMU-PS J213409.5-533631 'Dancing ghosts'
7b	309.5406	-52.0798	17642	> 99.7	NGC 6935 ringed face-on spiral galaxy
7c	332.1117	-57.4486	18983	> 99.9	NGC 7205 spiral galaxy
7d	327.9267	-55.3463	20670	> 99.9	FR-I extended radio source with host galaxy 2MASX J21512991-5520124
8a	312.0952	-49.1989	18944	> 99.9	2MASX J20483764-4911157 FR-II remnant, no core
8b	310.4449	-52.9070	18906	> 99.9	2MASX J20411202-5257379 FR-I, WAT
8c	328.8119	-59.1678	18185	> 99.8	2MASX J21551267-5909011 FR-I, WAT
8d	311.4652	-51.1902	20215	> 99.9	FR-I extended radio source with host galaxy 2MASX J20455226-5106267
9a	307.0931	-49.3744	17886	> 99.8	DES J202818.12-492408.4 FRI, potential Double-double radio galaxy
9b	335.0137	-60.0578	19108	> 99.9	DES J221933.46-600149.9 FR-I/II
9c	322.2268	-60.3774	18270	> 99.8	2MASX J21284113-6021568 bent tail galaxy
9d	321.8638	-60.0386	17913	> 99.8	NGC 7059 spiral galaxy

**Table A2.** List of complex and unusual non-overlapping frames from figure A1, with a complexity of 17,000 bytes or greater. Reference refers to a position in figure A1.

selected fractional percentile bins and provide a representation of the high value complexity tail and the diverse morphology found within.

This paper has been typeset from a  $\text{\TeX}/\text{\LaTeX}$  file prepared by the author.

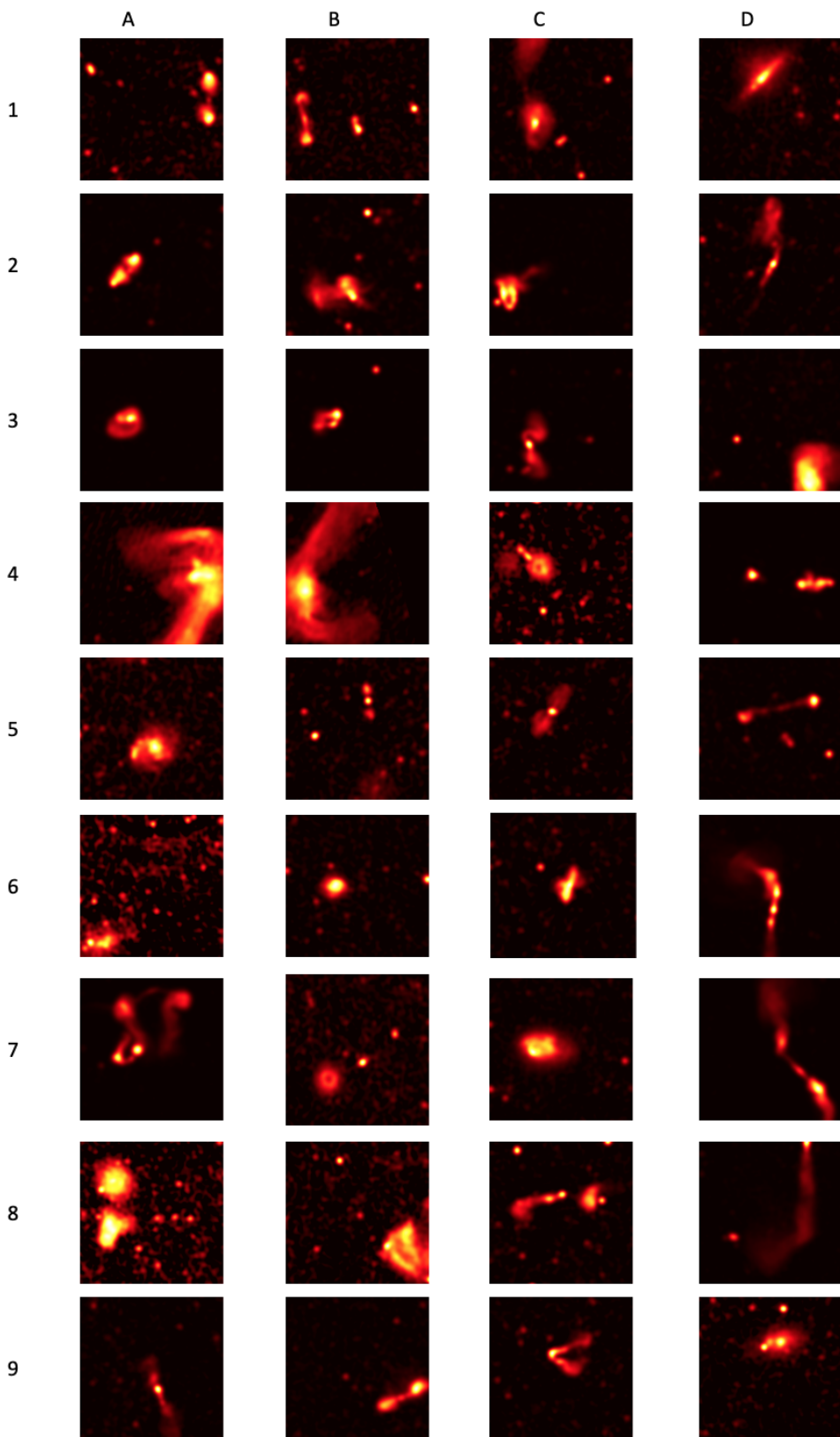


**Figure A1.** Examples of interesting non-overlapping frames with a complexity of 17,000 bytes or greater. Coordinates specify the location of the centre of each frame.